Measurement of 2-D Sea Surface Elevation Fields Using Complex Synthetic Aperture Radar Data

Johannes Schulz-Stellenfleth and Susanne Lehner, *Member, IEEE*

***Abstract*—A method is presented to derive two-dimensional sea surface elevation fields from complex synthetic aperture radar (SAR) data. Applied to spaceborne SAR data as acquired by European Remote Sensing 2 (ERS-2) or the Environmental Satellite (ENVISAT), the method allows to analyze the structure of ocean wave fields, e.g., wave grouping or individual wave heights on a global scale. The technique, thus, provides wave parameters not obtained with common SAR wave retrieval schemes, which are designed to estimate the 2-D wave spectrum, i.e., second-order statistical moments of the wave field. Estimates of sea surface elevation fields are obtained based on the existing theory of SAR ocean wave imaging, i.e., the modulation of the SAR image intensity due real aperture radar and motion-related effects. A power series expansion is derived for SAR intensity images that enables the analysis of nonlinear effects as well as to derive a quasi-linear approximation of the SAR imaging model in the spatial domain. A statistical analysis is performed based on a global dataset of 2-D wave spectra provided by the European Centre for Medium-Range Weather Forecast. Distributions are given for the relative error of the quasi-linear approximation in the spatial domain. It is shown that the error can be reduced by smoothing the SAR image in the azimuthal direction at the cost of lower resolution. Smoothed elevation fields are retrieved by the minimization of a cost function defined in the Fourier domain based on the quasi-linear approximation of the imaging process. A multilook technique is applied to infer the information on wave propagation directions, which is required because the SAR transfer function is non-Hermitian, i.e., the SAR image is not determined by the "frozen" sea surface, but wave motion has a significant impact. The method is applied to simulated SAR images as well as to data acquired by ERS-2. The errors of the retrieved wave field due to image noise, uncertainties in the SAR imaging model, and bandwidth limitations are analyzed. In particular, the fact that the estimated elevation field is smoothed due to the finite system resolution and smearing effects associated with wave motion is discussed. A statistical test is proposed to check the homogeneity of the SAR image. The method makes sure that atmospheric effects are not misinterpreted as being caused by ocean waves.**

***Index Terms*—Individual waves, ocean waves, sea surface elevation, synthetic aperture radar (SAR).**

I. INTRODUCTION

IT HAS BEEN amply demonstrated that synthetic aperture radar (SAR) data can be used to estimate parameters of the two-dimensional (2-D) sea surface elevation field [1]–[7]. Due to their high spatial resolution and all-weather and daylight capabilities, spaceborne SAR systems are the only sensors that can provide directional ocean wave information on a continuous and global scale.

Manuscript received March 3, 2003; revised December 24, 2003. This work was supported by the European Union under the framework of the MAXWAVE Project.

The authors are with the Remote Sensing Technology Institute, German Aerospace Center (DLR), D-82234 Wessling, Germany (e-mail: johannes.schulz-stellenfleth@dlr.de).

Digital Object Identifier 10.1109/TGRS.2004.826811

Traditionally, SAR ocean wave measurements were carried out in the spectral domain using SAR image variance spectra to estimate 2-D ocean wave spectra [8]–[10]. This approach was later extended to SAR look cross spectra, which make use of the special SAR imaging process, to retrieve wave propagation directions without ambiguity [11]. Although the spectral approach is appropriate in particular for applications like wave model assimilation [12], it disregards a lot of detailed information on the 2-D sea surface elevation field provided by SAR.

The objective of this paper is to present a new technique, which provides estimates of the sea surface elevation field from complex SAR data. The method can be understood as complementary to traditional retrieval schemes, which provide estimates of the respective second-order statistical moment given by the wave spectrum. The estimated wave fields offer new applications of SAR data in ocean wave research and wave forecast, as in the following, for example:

- analysis of individual waves, e.g., freak waves;
- statistical analysis of maximum wave heights and resulting exceedence probabilities;
- analysis of wave grouping;
- estimation of statistical moments higher than second order;
- analysis of inhomogeneous wave fields.

Apart from additional information on the ocean wave field, the use of the full image information also helps to improve the understanding of the SAR imaging process. The knowledge about the general statistics of the sea surface elevation [13] or wave maxima can, for example, be used to fine-tune the radar transfer functions.

To measure sea surface elevation fields from SAR data, we take a classical retrieval approach based on a quasi-linear model for the imaging process. The idea is to find that wave field that minimizes the deviations between the simulated and the observed SAR image. The problem has an additional complexity due to the fact that the SAR image is not determined by the "frozen" sea surface alone, but information about the complex wave spectrum is required. In particular, the SAR image depends on the wave propagation directions, which can be extracted from a single SAR image, but only with 180° ambiguity. To infer the required information on wave motion, a multilook technique is used that provides two SAR images with a time separation Δt in the order of 0.5 s for typical spaceborne SAR systems. With the complex wave spectrum as the unknown quantity and the complex Fourier transforms of the two looks as the measurement, the retrieval problem has a unique solution, at least in spectral regimes where the magnitude of the SAR modulation transfer function (MTF) is not too small.

The SAR ocean wave imaging process has been analyzed in many studies and is quite well understood by now. The modulation of the SAR image intensity is caused by both real aperture radar (RAR) effects and motion-related mechanisms [3]. Whereas the RAR mechanism is well described by linear models, the velocity bunching effect can be strongly nonlinear for shorter waves traveling in the sensor flight direction (azimuth). The bunching effect can lead to strong distortions of the spectrum, which are outside the linear regime. In particular, it leads to the azimuthal cutoff, i.e., information loss on short azimuth traveling waves. In the nonlinear regime, the inversion problem becomes much more complicated, mainly because of the coupling of different wave components introduced by the higher order terms of the imaging process. In spectral inversion schemes as proposed in [9], *a priori* information on spectral densities, e.g., taken from numerical ocean wave models, can be used to deal with coupling of wave components, which are captured by the measurement, and those lost due to the velocity bunching mechanism. However, for the inversion in the spatial domain, this approach is not feasible, as it would require knowledge not only about spectral densities but also about the respective phases, which are not provided by common wave models.

The approach taken in this study is to restrict the retrieval to the lower wavenumber regime, i.e., the proposed scheme provides estimates of elevation fields that are smoothed in the azimuthal direction. It is shown that nonlinear image features can be reduced significantly by smoothing of the SAR data. This procedure makes the use of a quasi-linear inversion method feasible at the cost of a reduced azimuthal resolution of the retrieved elevation fields. A quasi-linear approximation has already been successfully used for wave spectra retrieval from SAR data [14].

The paper is structured as follows. In Section II, we review the basic SAR ocean wave imaging mechanisms that have to be taken into account in wave field estimation. An integral expression is derived, which allows to express the SAR intensity image as a power series with respect to the underlying wave field. A quasi-linear expression for the SAR intensity image is derived and compared to the full nonlinear transform based on a global dataset of ECMWF wave model spectra. Section III is about the cross-spectra technique, which is later used to resolve the wave propagation direction without ambiguity. Section IV summarizes some basic noise properties of SAR data, which are later used to estimate errors in the resulting elevation fields. In Section V, the inversion method to derive 2-D sea surface elevation fields from complex SAR data is introduced. In Section VI, the errors due to lowpass filtering, image speckle noise, and uncertainties in the SAR imaging model are analyzed.

II. SAR Ocean Wave Imaging Theory

SAR imaging of ocean waves has been analyzed in many studies [1]–[5], [15]. It has been shown that for incidence angles between 20° and 60°, the process is dominated by two mechanisms [3] as follows:

- modulation of the radar cross section (RCS) by long waves, i.e., waves longer than the SAR resolution cell (this is commonly referred to as real aperture radar (RAR) modulation);
- Doppler shifts associated with the orbital motion of the ocean waves (the resulting effect on SAR imagery is usually called velocity bunching).

The RAR modulation I^R of the normalized RCS σ_0 is usually described by a linear model, which is based on a Fourier representation of the sea surface elevation η at time t

$$\eta(\mathbf{x},t) = 2\mathrm{Re}\left(\sum_{\mathbf{k}} \eta_{\mathbf{k}} \exp[i\,(\mathbf{kx} - \omega_{\mathbf{k}} t)]\right). \tag{1}$$

Here, Re denotes the real part, $\mathbf{k}$ is the 2-D wavenumber vector, η_k are the complex Fourier coefficients of the sea surface, and $\omega_{\mathbf{k}}$ is the angular wave frequency. For deep water, $\omega_{\mathbf{k}}$ is connected to the wavenumber via the dispersion relation $\omega_{\mathbf{k}} = (gk)^{1/2}$ with gravitational acceleration g [16].

The modulation of the normalized RCS can then be written as

$$\begin{aligned} I^R(\mathbf{x},t) &= \frac{\sigma_0(\mathbf{x},t) - \langle\sigma_0\rangle}{\langle\sigma_0\rangle} \\ &= 2\mathrm{Re}\left(\sum_{\mathbf{k}} T^R_{\mathbf{k}} \eta_{\mathbf{k}} \exp[i\,(\mathbf{kx} - \omega_{\mathbf{k}} t)]\right). \end{aligned} \tag{2}$$

Here, T^R is the RAR MTF, which is governed by different geometrical and hydrodynamic mechanisms [3]. The corresponding analytical expressions used in this study can be found in Appendix A. It should be noted that there is still some uncertainty about the exact phase and magnitude of the RAR MTF [17]. Furthermore, there are different approaches to include a possible wind dependence. However, as the focus of this study is on the inversion procedure, which can be carried out with any MTF, we will use the relatively simple expressions in Appendix A and leave it to the individual users of the method to choose their favorite MTF.

A SAR uses the Doppler shifts of the returned signals to achieve its high resolution in flight direction (azimuth) [18]. In standard SAR processing, it is assumed that the imaged scene is stationary, which, in general, is not the case for an ocean surface. A slant range component u_r of the orbital velocity causes a shift $\xi = RV^{-1}u_r$ of the respective image point in the azimuth direction, where R is slant range and V is the platform velocity [1]. In a linear approximation, u_r can be expressed in terms of the wave spectrum as

$$u_r(\mathbf{x},t) = 2\mathrm{Re}\left(\sum_{\mathbf{k}} T^u_{\mathbf{k}} \eta_{\mathbf{k}} \exp[i\mathbf{kx} - \omega_{\mathbf{k}} t]\right) \tag{3}$$

where $T^u_{\mathbf{k}}$ is the orbital velocity transfer function given by

$$T^u_{\mathbf{k}} = -\omega_{\mathbf{k}}\left(\frac{k_y}{|k|}\sin\theta + i\cos\theta\right) \tag{4}$$

with incidence angle θ.

Based on (2) and (3), the following integral expression can be derived for a SAR image I^S of a moving sea surface [19]

$$\begin{aligned} I^S(\mathbf{x}) + 1 = \frac{\sqrt{\pi}}{2\,\rho_a} &\int (1 + I^R(\mathbf{x}')) \\ &\cdot \exp\left[-\frac{\pi^2}{4\rho_a^2}(x - x' - \xi(\mathbf{x}'))^2\right]\delta(y' - y)\,dx'\,dy' \end{aligned} \tag{5}$$

TABLE I
COMPARISON OF DIFFERENT ENVISAT ASAR AND ERS SAR WAVE MODE PARAMETERS OF SINGLE-LOOK COMPLEX IMAGES

	ERS-1/2	ENVISAT
radar frequency	C Band	C Band
polarization	VV	HH or VV
incidence angle θ	23.5°	14.1° - 42.3°
$R\,V^{-1}$	111.5 s	108 s - 142 s
ρ_a	$\approx$ 10 m	$\approx$ 10 m
ρ_r	$\approx$ 10 m	$\approx$ 10 m
look direction	right	right
Δt	0.7 s	0.7 s

where ρ_a is the system resolution in the azimuth direction, and x and y are the spatial coordinates in azimuth and range, respectively. An important property of the transform (5) is that it maintains the mean intensity, i.e., $\langle I^S \rangle = \langle I^R \rangle = 0$ [5].

To analyze the nonlinearity of the imaging process and to derive a quasi-linear approximation, it is helpful to take the Fourier transform (denoted by $\mathcal{F}$) of each of the azimuth lines in (5). Applying a variable transform and integrating out the exponential function, one obtains

$$\mathcal{F}(I^S(y)+1) = \exp\left[-\frac{\rho_a^2}{\pi^2}k_x^2\right]\int dx \cdot \exp[-i(k_x\,x+\xi(\mathbf{x})k_x)](1+I^R(\mathbf{x})). \quad (6)$$

Expanding the exponential function under the integral in a power series and ordering the terms with increasing nonlinearity order with respect to the underlying ocean wave field yields

$$\mathcal{F}(I^S(y)) = \exp\left[-\frac{\rho_a^2}{\pi^2}k_x^2\right]\sum_{n=1}^{\infty} a_n(I^R,\xi,k_x) \quad (7)$$

with functions a_n defined as follows:

$$a_n(I^R,\xi,k_x) = \int dx\,\exp[-ik_x\,x] \cdot \frac{(-ik_x\xi(\mathbf{x}))^{n-1}}{(n-1)!}\left(I^R(\mathbf{x}) - \frac{ik_x}{n}\xi(\mathbf{x})\right). \quad (8)$$

For the ENVISAT imaging configuration (compare Table I), the expansion typically requires 50 terms or more before convergence occurs, reflecting the strong nonlinearity of the mapping process. Here, convergence is defined as the nonlinearity order at which the image variance contribution of the corresponding expansion term is less than 1% of the respective contribution of the linear $(n=1)$ term.

The highest nonlinearities in the SAR image are associated with shorter azimuth traveling waves. In order to make the quasi-linear inversion procedure presented in Section V feasible, our approach is to smooth these waves out. The size of the smoothing window is defined in terms of the estimated azimuthal cutoff wavelength λ_{cut}. The cutoff wavelength of the SAR image is estimated by fitting a Gaussian

$$C(x) = \exp\left[-\frac{\pi^2 x^2}{\lambda_{\mathrm{cut}}^2}\right] \quad (9)$$

to the respective azimuthal autocorrelation function [20]. The smoothed SAR image $\overline{I}^S$ is then defined as

$$\mathcal{F}(\bar{I}^S(y)) = \mathcal{F}(I^S(y))\exp\left[-k_x^2\lambda_{\mathrm{cut}}^2(\kappa^2-1)\right] \quad (10)$$

where the new cutoff wavelength λ_s is given by

$$\lambda_s = \kappa\lambda_{\mathrm{cut}} \quad (11)$$

with a parameter $\kappa \geq 1$.

To quantify the impact of the smoothing process, a global dataset of 1000 2-D ECMWF wave spectra was used for Monte Carlo simulations. For each of the spectra, a realization of a surface elevation field and a corresponding orbital velocity field was calculated with a random generator assuming uniformly distributed phases of the complex wave spectrum. These two fields were then used as input for the transform (10). Histograms of the required expansion terms of the Taylor series are given in Fig. 7(B) for different values of κ. As one can see, the smoothing operation reduces the order of nonlinearity considerably. The corresponding effective azimuthal cutoff wavelength λ_s is given in Fig. 7(C). The respective ratio of the cutoff waveheight H_{cut}, and the significant waveheight H_s is given in Fig. 7(D). Here, H_{cut} is defined as

$$H_{\mathrm{cut}}^2 = 16\int_{|k_x|<2\pi\lambda_s^{-1}} F_{\mathbf{k}}d\mathbf{k} \quad (12)$$

where $F_{\mathbf{k}}$ is the 2-D wave spectrum in the wavenumber domain defined as

$$F_{\mathbf{k}}d\mathbf{k} = 2\langle|\eta_{\mathbf{k}}|^2\rangle \quad (13)$$

where $d\mathbf{k}$ is the spectral bin size associated with the finite surface area considered. If the ratio is equal to one, no spectral energy is lost due the smoothing, whereas all energy is smoothed out if the ratio is zero.

Due to the reduced nonlinearity, it makes sense to use a linear approximation for the smoothed SAR image. Furthermore, it is possible to derive a quasi-linear approximation by splitting the wave spectrum into one part with azimuth waves longer than the cutoff wavelength λ_s and a second part with the remaining components. Accordingly, we write ξ and I^R as

$$\xi = \xi_l + \xi_h \quad I^R = I_l^R + I_h^R$$

where ξ_l, I_l^R refer to the low azimuth wavenumber part and ξ_h, I_h^R represent the shorter azimuth waves. The idea is to deal with short azimuth wave components, for which no phase information is available from the SAR data, by taking the average over all possible realizations. In this case, only information about the variance spectrum of these waves is required, which can be either taken from prior knowledge, e.g., numerical wave models, or empirical relationships with the azimuthal cutoff wavelength.

The quasi-linear transform is obtained by averaging the transform (6) over the short azimuth waves. Taking into account that the RAR modulation mechanism has a minor influence for these waves [4], a good approximation is obtained by averaging over ξ_h. Using the general relationship

$$\langle\exp[tX]\rangle = \exp[-0.5t^2\mathrm{var}(X)] \quad (14)$$

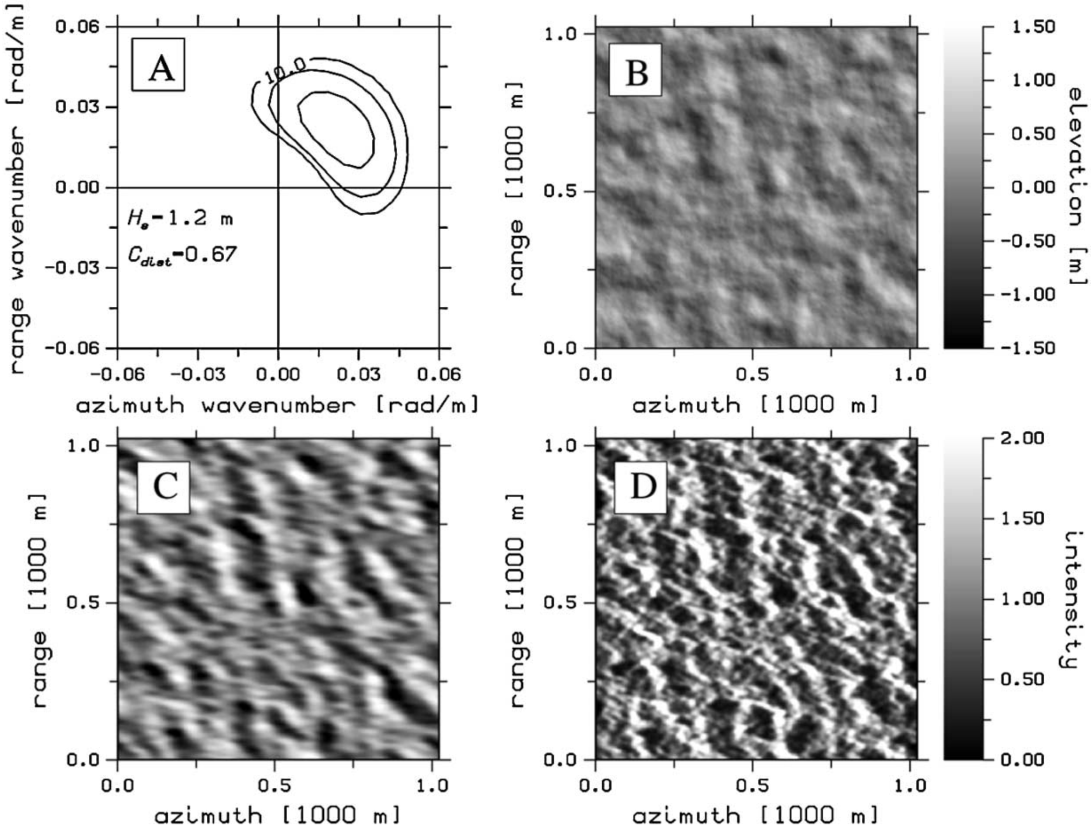

Fig. 1. Simulation of a SAR intensity image I^S using the full nonlinear (D) and quasi-linear (C) forward model given by (5) and (16), respectively. A JONSWAP spectrum (A) was used to simulate the respective ocean wave field (B) assuming uniformly distributed phases.

for a zero-mean Gaussian variables X and an arbitrary complex number t [5], one obtains the following expression:

$$\langle \mathcal{F}(\bar{I}^S)\rangle_{\xi_h} \approx \exp\left[-k_x^2\left(\frac{1}{2}\langle\xi_h^2\rangle + \lambda_{\text{cut}}^2(\kappa^2-1) + \frac{\rho_a^2}{\pi^2}\right)\right] \cdot \sum_{n=1}^{\infty} a_n(I_l^R, \xi_l, k_x). \quad (15)$$

Fig. 6 shows a scatterplot of $\langle\xi_h^2\rangle^{1/2}$ versus the cutoff wavelength λ_{cut} for $\kappa = 2$ [Fig. 6(A)] and $\kappa = 3$ [Fig. 6(B)]. One can see that the correlation is over 0.9 in both cases, which means that the average impact of the shorter azimuth waves can be well estimated from the cutoff wavelength.

Terminating this expansion after the linear term $(n = 1)$ yields the quasi-linear approximation for the smoothed SAR image, which can be written as

$$\mathcal{F}(\bar{I}^S) \approx \langle \mathcal{F}(\bar{I}^S)\rangle_{\xi_h} \approx \mathcal{F}(\bar{I}^{QS}) = T_{\mathbf{k}}^S \eta_{\mathbf{k}} + (T_{-\mathbf{k}}^S \eta_{-\mathbf{k}})^* \quad (16)$$

where $\mathcal{F}$ denotes the 2-D Fourier transform, and the SAR transfer function T^S is defined as

$$T_{\mathbf{k}}^S = \exp\left[-k_x^2\left(\frac{1}{2}\langle\xi_h^2\rangle + \lambda_{\text{cut}}^2(\kappa^2-1) + \frac{\rho_a^2}{\pi^2}\right)\right] \cdot \left(T_{\mathbf{k}}^R - ik_x\frac{R}{V}T_{\mathbf{k}}^u\right) \quad (17)$$

with k_x denoting the azimuth component of the wavenumber vector. Fig. 1 shows a comparison of the full nonlinear and quasi-linear transform for a wave field generated from a parametric Joint North Sea Wave Project (JONSWAP) [16] wave spectrum [Fig. 1(A)]. The ERS-2 imaging parameters as given in Table I were used for the simulation. The quasi-linear approximation of the intensity image is shown in Fig. 1(C), whereas Fig. 1(D) shows the full nonlinear image. One can see that the overall agreement is reasonable in this case with some differences caused by higher harmonics in the nonlinear transform, which are not captured by the quasi-linear model. A more detailed analysis of the errors of the quasi-linear approximation will be given at the end of this section.

Magnitude and phase of $T_{\mathbf{k}}^S$ for $\langle\xi_h^2\rangle = 5000$ m^2 and $\kappa = 1$ are given in Fig. 2. One can see that the transfer function is non-Hermitian, i.e., $T_k^S \neq (T_{-k}^S)^*$. As can be seen from Appendix A and (17), the asymmetry is due to both the hydrodynamic modulation and the velocity bunching effect. The main consequence is that SAR, in general, does not act as a linear operator on the "frozen" sea surface, but the intensity image is a function of the complete complex wave spectrum. For instance, if a wrong propagation direction is assumed for an azimuth traveling wave, the predicted phase starting from the intensity image would be wrong by 180°.

For a single wave system propagating in the azimuth direction, the SAR imaging process can be expressed in the spatial domain as a convolution of the ocean wave field with the impulse response function H^1 shown in Fig. 2(C). The respective convolution kernel H^{-1} for a system propagating in the opposite flight direction is depicted in Fig. 3(D). H^1 and H^{-1} are

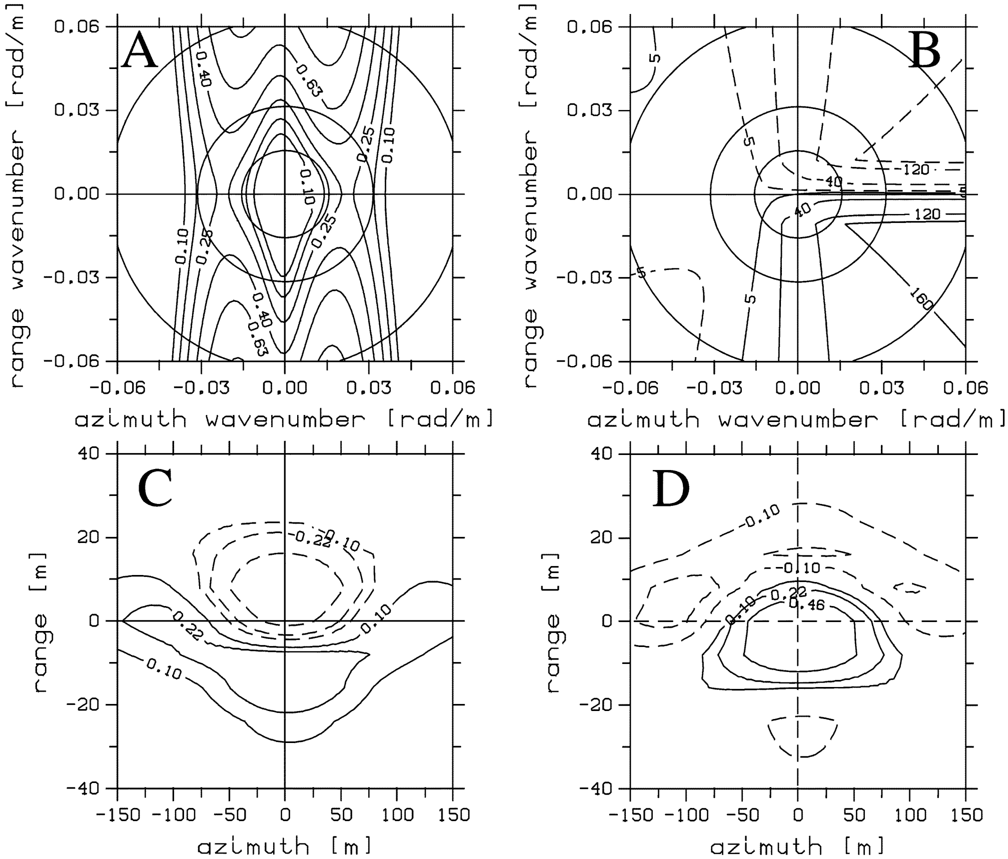

Fig. 2. (A) Modulus and (B) phase of the SAR transfer function T^{S} with orbital velocity variance $\langle u_r^2 \rangle = 0.5\ \mathrm{m}^2 \cdot \mathrm{s}^{-2}$. Isoline labels are given in units per square meter. SAR imaging parameters as given in Table I are assumed. Corresponding impulse response functions H^1, H^2 (normalized) describing the SAR imaging process in the spatial domain for a wave system traveling in (C) flight direction and (D) in opposite flight direction. Dashed contour lines indicate negative values.

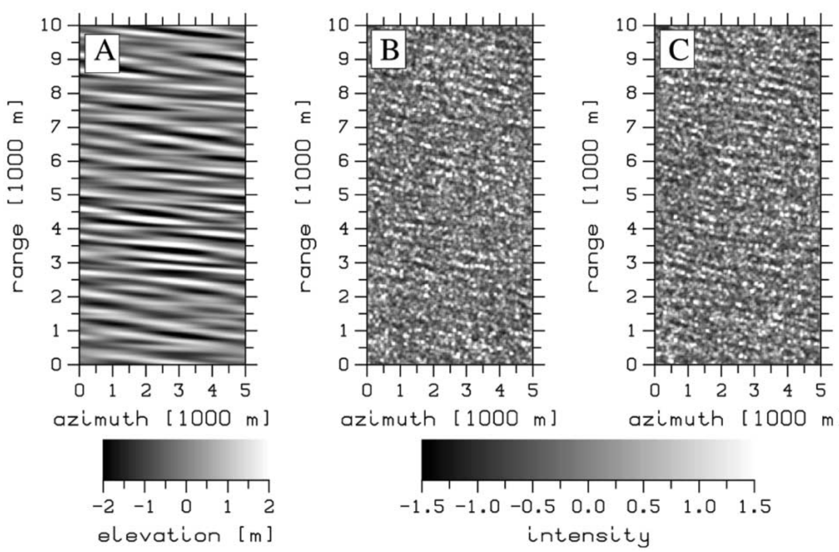

Fig. 3. (A) Sea surface elevation field derived from an ERS-2 wave mode imagette acquired at 59.2° S 102.1° E on June 1, 1997, 8:27 UTC. (B), (C) Two looks I^-, I^+ with time separation of $\Delta t = 0.33$ s processed from the respective complex image used for the inversion procedure.

calculated as the Fourier transforms of the modified transfer functions

$$T_k^l = \begin{cases} T_k^S, & lk_x \geq 0 \\ (T_{-k}^S)^*, & lk_x \leq 0 \end{cases} l = -1, 1. \tag{18}$$

As anticipated, the imaging process is local (i.e., on the SAR resolution scale, which was assumed to be 30 m for the simulation) in the range direction. In the azimuth direction, the width of the convolution kernel is usually much larger depending on the orbital velocity variance and the R over V ratio of the system.

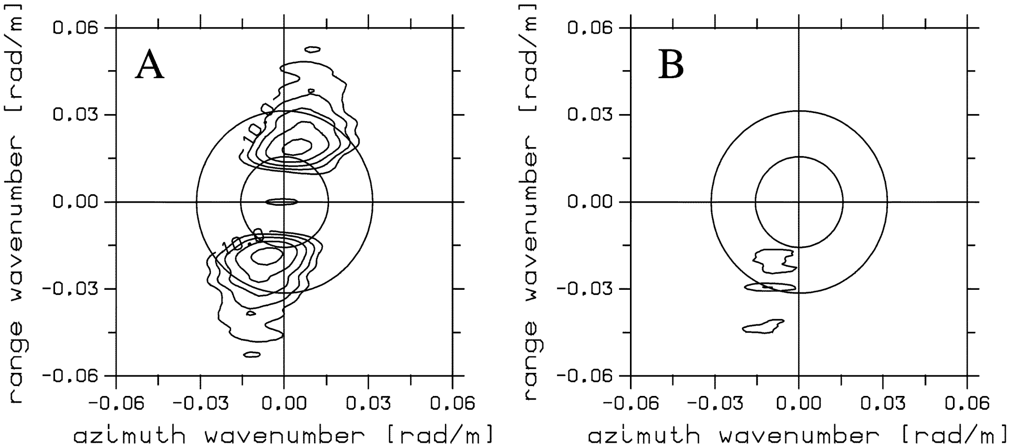

Fig. 4. (A) Real part and (B) imaginary part of the cross spectrum $\Phi^{L_1 L_2}$ computed from the two looks shown in Fig. 3.

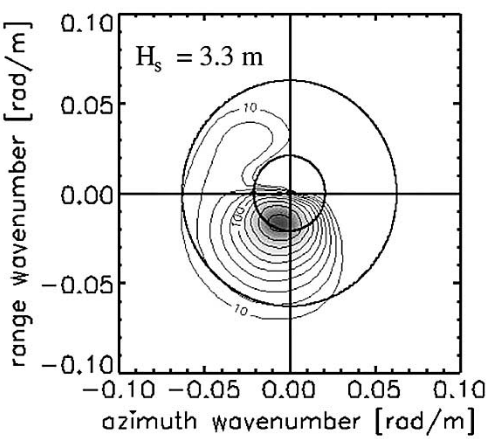

Fig. 5. Ocean wave model spectrum colocated with the ERS-2 imagette shown in Fig. 3(B) and (C).

The higher linearity achieved by smoothing of the SAR image is reflected by a reduction of the relative error of the quasi-linear transform (16) defined as

$$\rho_{\rm rel}^2 = \frac{\langle (\bar{I}^{QS} - \bar{I}^S)^2 \rangle}{\langle (\bar{I}^S)^2 \rangle} \tag{19}$$

where the angle brackets indicate spatial averages. Fig. 7(A) shows the distribution of the error $\rho_{\rm rel}$ estimated from the global dataset of ECMWF spectra for different values of κ. One can see that the error of the quasi-linear transform can be reduced significantly by smoothing of the SAR image in the azimuth direction.

III. Multilook Technique

As shown in the previous section, SAR retrieval of ocean wave fields requires information on wave propagation directions. In this section, a technique is summarized that is able to retrieve this information from complex SAR data. Complex SAR data contain information on the time evolution of the RCS during the integration time T_0, which is typically in the order of 1 s for spaceborne civilian C-band SAR systems. This information can be extracted by applying the so-called multilook technique. In this method, the integration time is split in two or more subintervals, and each interval is processed to a SAR image separately. Denoting the so-called Doppler centroid time with $t_{\rm dc}$ [18] one can generate two looks

$$I^- = I^S(t_{\rm dc} - 0.5\Delta t) \tag{20}$$

$$I^+ = I^S(t_{\rm dc} + 0.5\Delta t) \tag{21}$$

with time separation $\Delta t \approx 0.5 T_0$. In the case of ocean waves, the shift of wave patterns on the looks can then be used to gain information about the respective propagation directions. Commonly, the phase shift is estimated using cross spectra. The cross spectrum is defined as

$$\Phi_{\mathbf{k}}^{I^- I^+} = \langle \zeta_{\mathbf{k}}^- (\zeta_{\mathbf{k}}^+)^* \rangle \tag{22}$$

where $\zeta_{\mathbf{k}}^-, \zeta_{\mathbf{k}}^+$ are the complex Fourier transforms of the two looks, and the asterisk denotes complex conjugation. Fig. 4 shows the cross spectrum derived from the looks in Fig. 3. The wave propagation direction is indicated by the positive peak of the imaginary part.

IV. Noise Model

The SAR intensity image I^S given by (5) is idealized because it does not contain image noise. In practice, one has a SAR image $\hat{I}^S$ that is affected by so-called speckle noise [21]. In the commonly used multiplicative noise model [18], the estimated intensity $\hat{I}^S$ is expressed as the product of a negative exponential distributed speckle process S with unit mean and a process I^S carrying the RCS information [22]. The two processes are assumed to be statistically independent. To first order, it can be assumed that the correlation length of the speckle S, which is on the SAR resolution scale, is shorter than the correlation length of the modulation I^S [20]. The variance spectrum $\Phi^{\hat{I}^S}$ of $\hat{I}^S$ can then be written as follows:

$$\Phi_{\mathbf{k}}^{\hat{I}^S} = \Phi_{\mathbf{k}}^{I^S} + \Phi_{\mathbf{k}}^S (1 + {\rm var}(I^S)) \approx \Phi_{\mathbf{k}}^{I^S} + \Phi_{\mathbf{k}}^S \tag{23}$$

where Φ^S is the variance spectrum of the speckle process S. As can be seen, the first-order impact of SAR image speckle on the normalized SAR image variance spectrum is an additional noise floor. The last approximation holds because the variance of the modulation I^S, caused by ocean waves, is in general much

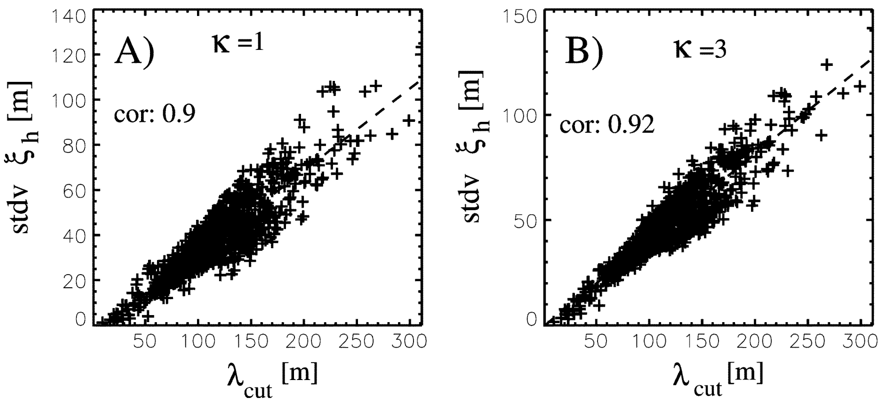

Fig. 6. Scatterplot of the standard deviation of the shift variable ξ_h [compare (14)] versus the cutoff wavelength λ_{cut} for (A) $\kappa = 1$ and (B) $\kappa = 3$.

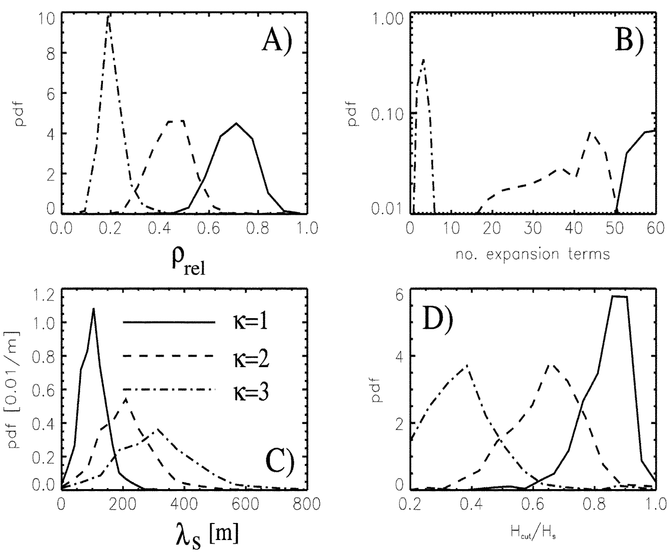

Fig. 7. (A) PDF of the relative error of the quasi-linear imaging model estimated from a global dataset of 1000 ECMWF wave model spectra for different sizes of the smoothing window [compare (10)]. ENVISAT imaging parameters were assumed for the simulation (compare Table I). (B) The same as (A) for the number of terms required in the Taylor expansion of the smoothed image. (C) Respective azimuthal cutoff wavelengths. (D) Ratio of the waveheight H_{cut} captured by the SAR to the waveheight H_s.

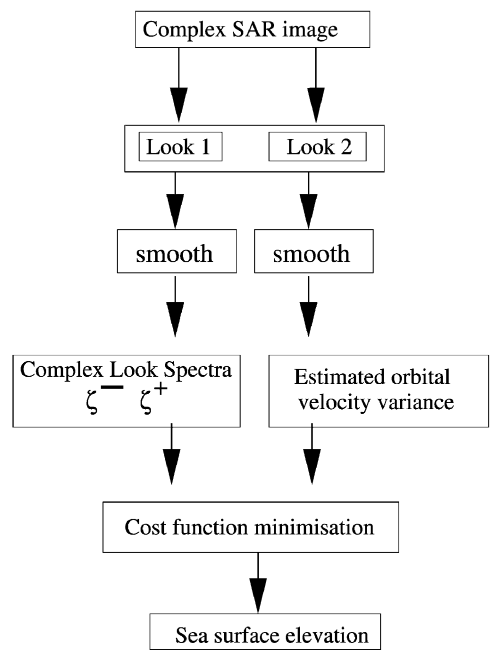

Fig. 8. Flowchart of the SAR retrieval scheme for sea surface elevation fields.

smaller than one [23]. Assuming white speckle noise and a SAR system with range and azimuth resolution ρ_{az} and ρ_{ra}, the noise floor is then approximately given by

$$\Phi_{\mathbf{k}}^{S} = \frac{\rho_{\text{az}}\rho_{\text{ra}}}{4\pi^2}. \tag{24}$$

Note that the speckle variance can be reduced at the cost of lower spatial resolution using multilook techniques.

For the retrieval scheme described in Section V, a noise model is needed for the complex image spectrum ζ_k. We assume that ζ_k is affected by additive circular Gaussian noise, i.e., identically distributed and independent real and imaginary part. Using (24), the variance of the complex spectrum $\zeta_{\mathbf{k}}^{S}$ is calculated as

$$\left(\sigma_{\mathbf{k}}^{S}\right)^2 = \left\langle \left|\zeta_{\mathbf{k}}^{S}\right|^2 \right\rangle = \Phi_{\mathbf{k}}^{S} d\mathbf{k}. \tag{25}$$

Note, that this variance refers to different realizations of the speckle noise process with the underlying cross-section modulation kept fixed. A model for a joint distribution of the complex spectra of two looks, based on an ensemble of different sea surface realizations, can be found in [24].

V. SAR Retrieval of Sea Surface Elevation Fields

As pointed out in Section II, a SAR image of ocean waves depends on the respective wave propagation directions. In order to measure sea surface elevation fields, we therefore have to infer information on wave evolution. The inversion scheme presented in this section is based on the idea to extract this information from complex SAR data. A flowchart of the method is given in Fig. 8. The method uses normalized SAR looks I^+, I^-, processed as described in Section III. As explained in Section II, it makes sense to smooth the looks in the azimuth direction to reduce nonlinearities, which cause errors in the quasi-linear inversion procedure. Furthermore, one has to make sure that the SAR data do not contain features that have nothing to do with ocean waves, e.g., rain cells or sea ice. A reliable method to detect such cases is described in Appendix B.

The respective complex Fourier transforms $\zeta_{\mathbf{k}}^{+}, \zeta_{\mathbf{k}}^{-}$ of the looks are calculated as

$$\zeta_{\mathbf{k}}^{+/-}(t) = \frac{1}{N_x N_y} \cdot \sum_{\mathbf{k}} \frac{I^{+/-}(\mathbf{x},t) - \langle I^{+/-}(y)\rangle}{\langle I^{+/-}(y)\rangle} \exp[-i\mathbf{k}\mathbf{x}] \quad (26)$$

where we have assumed that the SAR image has $N_x \times N_y$ pixels. For larger images, the mean intensity is not constant but decreases with increasing incidence angles in the far range [25]. This explains the explicit dependence of $\langle I^{+/-}(y)\rangle$ on the range coordinate y used in (26).

The complex spectra ζ^{+}, ζ^{-}, which contain the same information as the original images, are used as input for the inversion scheme. The quantity we want to measure is the complex wave spectrum $\eta_{\mathbf{k}}$. Using the quasi-linear forward model for the SAR imaging process introduced in Section II, $\zeta_{\mathbf{k}}^{+}$ and $\zeta_{\mathbf{k}}^{-}$ can be written as

$$\zeta_{\mathbf{k}}^{-} = n_{\mathbf{k}}\left(T_{\mathbf{k}}^{-}\eta_{\mathbf{k}} + (T_{-\mathbf{k}}^{-}\eta_{-\mathbf{k}})^*\right) + \epsilon_{\mathbf{k}}^{-} \quad (27)$$

$$\zeta_{\mathbf{k}}^{+} = n_{\mathbf{k}}\left(T_{\mathbf{k}}^{+}\eta_{\mathbf{k}} + (T_{-\mathbf{k}}^{+}\eta_{-\mathbf{k}})^*\right) + \epsilon_{\mathbf{k}}^{+}. \quad (28)$$

Here, we have assumed that the complex look spectra are affected by uncorrelated additive Gaussian noise $\epsilon_k^{-}, \epsilon_k^{+}$ associated with SAR image speckle with zero mean and variance given by (compare Section IV)

$$\left\langle \left|\epsilon_{\mathbf{k}}^{+}\right|^2 \right\rangle = \left\langle \left|\epsilon_{\mathbf{k}}^{-}\right|^2 \right\rangle = \left(\sigma_{\mathbf{k}}^{S}\right)^2. \quad (29)$$

Furthermore, we assume relative errors in the SAR imaging model represented by a Gaussian distributed complex variable $n_{\mathbf{k}}$ with unit mean and variance $(\sigma_{\mathbf{k}}^{n})^2$ (compare Fig. 10). The two error sources are taken as being statistically independent and have to fulfil

$$n_{\mathbf{k}} = n_{-\mathbf{k}}^* \quad (30)$$

$$\epsilon_{\mathbf{k}} = \epsilon_{-\mathbf{k}}^*. \quad (31)$$

The transfer functions $T_{\mathbf{k}}^{+}, T_{\mathbf{k}}^{-}$ in (27) and (28) are defined as

$$T_{\mathbf{k}}^{+} = T_{\mathbf{k}}^{S} \exp(-i0.5\Delta t\omega_{\mathbf{k}}) \quad (32)$$

$$T_{\mathbf{k}}^{-} = T_{\mathbf{k}}^{S} \exp(+i0.5\Delta t\omega_{\mathbf{k}}) \quad (33)$$

and take into account the wave phase shift occurring in the time Δt between the look acquisitions [compare (1)].

A maximum-likelihood estimate $\hat{\eta}_{\mathbf{k}}$ for given measurements $\zeta_{\mathbf{k}}^{-}, \zeta_{\mathbf{k}}^{+}$ is obtained by solving the system of (27) and (28) after averaging out the noise contributions. The result is given by

$$\widehat{\eta}_{\mathbf{k}} = d_{\mathbf{k}}^{-1}(\zeta_{\mathbf{k}}^{-}(T_{-\mathbf{k}}^{+})^* - \zeta_{\mathbf{k}}^{+}(T_{-\mathbf{k}}^{-})^*) \quad (34)$$

with determinant $d_{\mathbf{k}}$ defined as

$$\begin{aligned} d_{\mathbf{k}} &= T_{\mathbf{k}}^{-}(T_{-\mathbf{k}}^{+})^* - T_{\mathbf{k}}^{+}(T_{-\mathbf{k}}^{-})^* \\ &= 2\,i\sin(\Delta t\omega_{\mathbf{k}})T_{\mathbf{k}}^{S}\left(T_{-\mathbf{k}}^{S}\right)^*. \end{aligned} \quad (35)$$

As can be seen, $d_{\mathbf{k}}$ is zero if the look separation time Δt is zero, which means that the multilook technique is essential for the retrieval method. Due to the symmetric definition of the transfer functions, the wave spectrum $\hat{\eta}_{\mathbf{k}}$ in (34) refers to the ocean wave field at Doppler centroid time t_{dc}. The inverted elevation field $\bar{\eta}(\mathbf{x},t)$ at time t is calculated as

$$\bar{\eta}(\mathbf{x},t) = \sum_{\mathbf{k}\in Z} \bar{\eta}_{\mathbf{k}} \exp[i\,\mathbf{k}\,\mathbf{x}] \quad (36)$$

where the symmetric spectrum $\bar{\eta}_{\mathbf{k}}$ is given by

$$\bar{\eta}_{\mathbf{k}} = \hat{\eta}_{\mathbf{k}} + \hat{\eta}_{-\mathbf{k}}^* \quad (37)$$

and the spectral regime Z is chosen according to signal-to-noise consideration. A straightforward approach is to use the spectral regime with the highest energy in the SAR image spectrum, i.e., Z is defined as

$$Z = \{\mathbf{k} \text{ for which } |\zeta_{\mathbf{k}}^{+}(\zeta_{\mathbf{k}}^{-})^*| > \rho \max_{\mathbf{k}'} |\zeta_{\mathbf{k}'}^{+}(\zeta_{\mathbf{k}'}^{-})^*|\} \quad (38)$$

where ρ is a parameter with $0 < \rho < 1$. The resulting errors in the estimated elevation field depending on the choice of Z will be analyzed in Section VI.

A demonstration of the inversion method for synthetic data without noise is shown in Fig. 9. Looks showing a Gaussian wave group propagating in the exact range or azimuth direction are taken as input. Respective cuts are given in Fig. 9(A). A time separation Δt of 1 s was chosen to allow a visual distinction of the two curves. The respective 2-D look at time t_1 with wave group propagating in the range direction is shown in Fig. 9(B). The inverted wave fields obtained from (34) are given in Fig. 9(C) and (D). One can see that for the azimuth traveling case shown in Fig. 9(C), the inverted wave field is strongly dependent on the wave propagation direction. If the wave group is traveling in sensor flight direction ($t_1 < t_2$), the SAR image pattern is about 180° phase shifted with respect to the ocean wave field, whereas it is in phase in the opposite case. For the range traveling group depicted in Fig. 9(D), the phase shift is about 90°, regardless of the wave propagation direction.

Fig. 3(A) shows the elevation field calculated from the two looks shown in Fig. 3(B) and (C), applying the above method with $\rho = 0.2$ [compare (38)] and additional smoothing with $\kappa = 2$ [compare (10)].

VI. Error Estimation

In this section, different error sources affecting the retrieved wave field $\bar{\eta}(\mathbf{x})$ are analyzed. The following are the three main error contributions:

- missing information on short azimuth waves;
- SAR data noise;
- uncertainties in the forward model.

As all three error sources are basically independent, the resulting error of the retrieved wave field can be estimated as

$$(\sigma_{\bar{\eta}(\mathbf{x})})^2 = \left(\sigma_{\bar{\eta}(\mathbf{x})}^{\mathrm{cut}}\right)^2 + \left(\sigma_{\bar{\eta}(\mathbf{x})}^{S}\right)^2 + \left(\sigma_{\bar{\eta}(\mathbf{x})}^{F}\right)^2. \quad (39)$$

In the following, we discuss the three error contributions separately.

A. Smoothing Errors

Due to the azimuthal cutoff, the quasi-linear inversion method is in general not able to retrieve a complete complex wave spectrum $\overline{\eta_{\mathbf{k}}}$. It is obvious that this circumstance leads to errors in the resulting wave field.

If one has some additional information about the spectral energy contained in the high-frequency part of the spectrum,

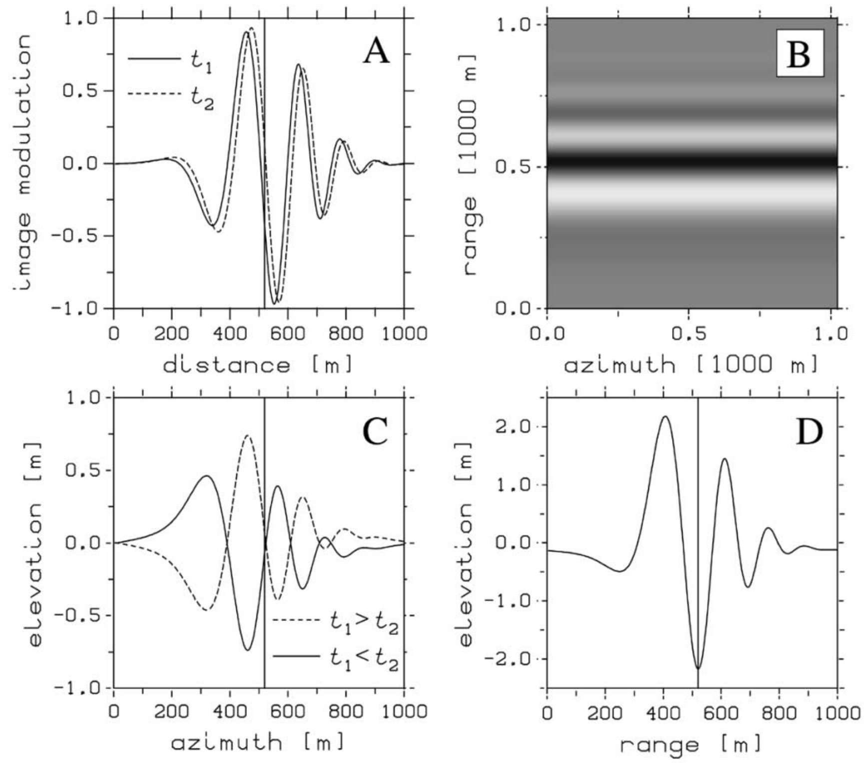

Fig. 9. Application of the inversion method to a Gaussian wave group (in deep water). (A) Looks taken at times t_1, t_2 with time separation of 1 s. (B) Two-dimensional look at time t_1 with wave group propagating in the range direction. (C) Inverted wave field assuming that the waves are propagating in (solid line) the positive or (dashed line) negative azimuth direction. (D) Inverted wave field assuming that the waves are propagating in the range direction.

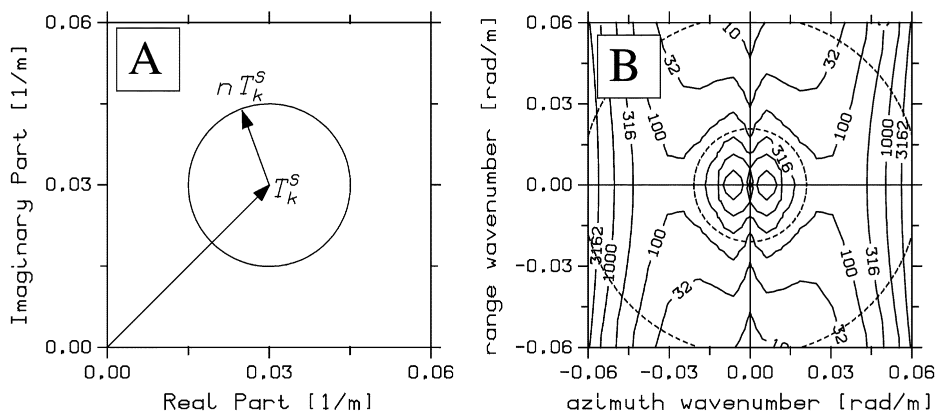

Fig. 10. (A) Illustration of the model used to take into account errors in the SAR transfer function [compare (27)]. The circle indicates the 65% confidence limit for $\sigma^n = 0.3$. (B) Variance spectrum of elevation errors associated with speckle noise [compare (44)].

e.g., from numerical models, one can define the respective wave height as

$$H_s^{Hf} = 4\sqrt{\int_{k \notin Z} F_{\mathbf{k}} d\mathbf{k}} \tag{40}$$

and the resulting standard deviation following from the fact that no phase information is available for these short waves is given by

$$\sigma_{\bar{\eta}(\mathbf{x})}^{\text{cut}} = \frac{1}{4} H_s^{Hf}. \tag{41}$$

If there is no prior information available. one has to accept the fact that the retrieved wave field does not represent the full wave spectrum. However, as the missing spectral components are well defined [compare (38)], the elevation still contains useful information in particular about the spatial structure of longer waves.

B. SAR Data Noise

It is obvious that the retrieval of wave energy according to (34) only makes sense for wavenumber vectors $\mathbf{k}$, which lead to reasonable SNRs of the resulting wave field. The variance of the spectral components $\bar{\eta}_{\mathbf{k}}$ due to image noise can be calculated as

$$\left(\sigma_{\bar{\eta}(\mathbf{k})}^S\right)^2 = \left(\sigma_{\mathbf{k}}^S\right)^2 \frac{|(T_{-\mathbf{k}}^+)^* - T_{\mathbf{k}}^+|^2 + |(T_{-\mathbf{k}}^-)^* - T_{\mathbf{k}}^-|^2}{|d_{\mathbf{k}}|^2}. \tag{42}$$

Here, we have used that $\langle \bar{\eta}_{\mathbf{k}} \bar{\eta}_{\mathbf{k}'} \rangle = 0$ for $\mathbf{k} \neq \mathbf{k}'$, which means that the error model given by (27) and (28) introduces homogeneous errors in the resulting wave field. Equation (42) shows that spectral regimes with small magnitude of the transfer function T^S are critical for the inversion, as the speckle noise is strongly amplified in this case.

The variance of the retrieved elevation field $\bar{\eta}(\mathbf{x})$ due to image noise follows as

$$\left(\sigma_{\bar{\eta}(\mathbf{x})}^S\right)^2 = \mathrm{var}(\bar{\eta}(\mathbf{x})) = \int_Z \Phi_{\mathbf{k}}^{\bar{\eta}} d\mathbf{k} \tag{43}$$

where the variance spectrum $\Phi^{\bar{\eta}}$ of the errors associated with speckle noise is given by

$$\Phi_{\mathbf{k}}^{\bar{\eta}} = \Phi_{\mathbf{k}}^S \frac{|(T_{-\mathbf{k}}^+)^* - T_{\mathbf{k}}^+|^2 + |(T_{-\mathbf{k}}^-)^* - T_{\mathbf{k}}^-|^2}{|d_{\mathbf{k}}|^2}. \tag{44}$$

Here, we have assumed again that a subset Z of wave components is selected to compose the wave field.

A contourplot of the variance spectrum (44), which represents errors of the estimated elevation field due to speckle noise, is shown in Fig. 10. The SAR transfer function T^S with $\langle \xi_h^2 \rangle = 5000\ \mathrm{m}^2$, $\kappa = 1$, and the ERS-2 resolution was assumed for the plot. As can be seen, the highest spectral density of the error is found for short waves traveling in the azimuth direction as well as for very long waves. If the entire spectral regime between 100-m wavelength and 300-m wavelength indicated by the dashed circles is used in the inversion, the resulting standard deviation of the elevation field due to speckle is about 2.4 m. However, it is clear that the spectral regime, e.g., defined by (38), is in general much smaller and thus the expected error significantly lower.

C. Errors in the Forward Model

The variance of the estimated complex wave spectrum due to errors in the forward model is given by

$$\left(\sigma_{\bar{\eta}(\mathbf{k})}^F\right)^2 = (\sigma_{\mathbf{k}}^n)^2 \, |\bar{\eta}_{\mathbf{k}}|^2. \tag{45}$$

The resulting error in the elevation field follows as

$$\left(\sigma_{\bar{\eta}(\mathbf{x})}^F\right)^2 = \mathrm{var}(\bar{\eta}(\mathbf{x})) = (\sigma_{\mathbf{k}}^n)^2 \int_Z F_{\mathbf{k}} d\mathbf{k} \tag{46}$$

where $F_{\mathbf{k}}$ is the "true" wave spectrum.

For the inversion example shown in Fig. 3, the numerical wave model (WAM) [31] gives a significant wave height of 3.3 m (compare Fig. 5). If we assume 30% error in the forward model, i.e., $\sigma^n = 0.3$, then the respective elevation variance is 0.06 m^2. The variance caused by speckle is 0.1 m^2 in this case. As explained before, this variance could be reduced using multilook techniques, which reduce the spatial resolution. The expected error due to uncertainties in the forward model and speckle noise is thus 0.4 m in this case.

VII. Conclusion

A new retrieval method has been presented that is able to provide estimates of smoothed 2-D wave fields from complex SAR data. The method, for the first time, allows spaceborne measurements of the structure of wave fields. It is in effect an extension of existing methods that provide only measurements of the ocean wave spectrum, i.e., statistical moments of the spatially averaged wave field.

A power series expansion was derived for SAR intensity images with respect to the underlying ocean wave field. Based on this expansion, the nonlinearity of the imaging process was analyzed. It was shown that nonlinear image features can be reduced by smoothing the SAR image in the azimuth direction at the cost of lower spatial resolution.

A quasi-linear approximation was derived for smoothed SAR images. Using a global dataset of ECMWF spectra, it was shown that the relative error of this approximation is reasonable, depending on the amount of smoothing.

Finally, an inversion procedure was proposed, based on the quasi-linear imaging model. In order to resolve the ambiguity of propagation direction present in single SAR images, a multilook technique was applied.

Statistical models were introduced to quantify the errors caused by both image noise and uncertainties in the SAR imaging forward model. Depending on the number of spectral components used to to compose the final wave field, error bars are provided for the surface elevation. As an option, *a priori* knowledge about the significant wave height (e.g., taken from numerical wave models) can be used as additional information.

Different approaches are currently taken to validate the proposed method with *in situ* data, e.g., laser as well as data acquired by other ground-based sensors, e.g., such as nautical radar. Comparing the different datasets will allow to fine tune both the phase and magnitude of the SAR transfer function as well as to estimate error bars for the retrieved elevation fields.

The application of the method to complex wave mode data provided by ENVISAT will allow a statistical analysis of wave parameters, like maximum to significant wave height ratios or wave grouping on a global scale. It is expected that such an analysis will give new insight into different aspects of ocean wave physics like the generation of extreme waves. To reach this goal, some further studies have to be performed, analyzing the detectability of extreme waves in smoothed elevation fields.

Appendix A

The real aperture radar MTF T^R, which is one component of the SAR MTF given by (17), can be expressed as the sum of three components, representing different independent physical mechanism [4]

$$T_{\mathbf{k}}^R = T_{\mathbf{k}}^{\mathrm{tilt}} + T_{\mathbf{k}}^{\mathrm{hydr}} + T_{\mathbf{k}}^{\mathrm{rb}}. \tag{47}$$

Here, T^{tilt} represents tilt modulation, T^{hydr} hydrodynamic modulation, and T^{rb} range bunching [4]. For vertical polarization in transmit and receive (VV) and a right looking SAR, analytical expressions for the transfer functions are given by

$$T_{\mathbf{k}}^{\mathrm{tilt}} = -\frac{4ik_y \cot\theta}{1+\sin^2\theta} \tag{48}$$

$$T_{\mathbf{k}}^{\mathrm{rb}} = -ik_y \cos\theta \sin\theta \tag{49}$$

$$T_{\mathbf{k}}^{\mathrm{hyd}} = 4.5\omega_{\mathbf{k}} \frac{k_y^2}{|k|} \frac{\omega_{\mathbf{k}} - i\mu}{\omega_{\mathbf{k}}^2 + \mu^2}. \tag{50}$$

Here, θ is the incidence angle, and μ is the hydrodynamic relaxation rate, which was set to $0.5s^{-1}$ in the open water [4]. The k_x and k_y components refer to a right-handed coordinate system with k_x pointing in the flight direction.

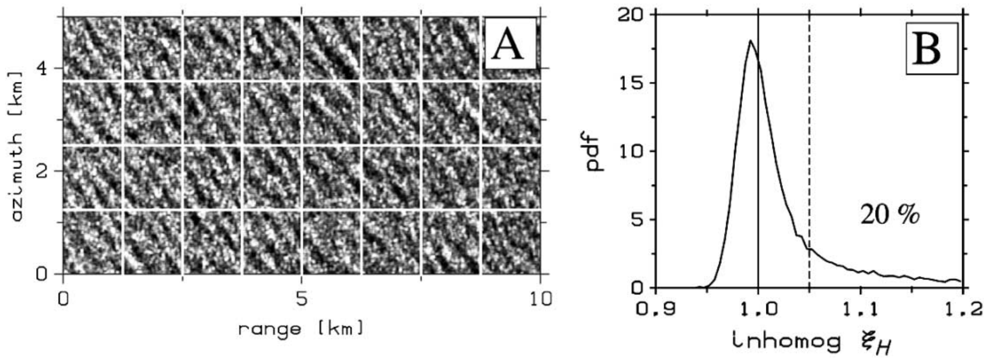

Fig. 11. (A) Boxes used to estimate the inhomogeneity parameter from wave mode imagettes. (B) Histogram of the inhomogeneity parameter estimated from a global dataset of 30 000 imagettes including land and sea ice.

APPENDIX B
TEST OF IMAGE HOMOGENEITY

On a spatial scale of a few kilometers, ocean wave fields should be approximately homogeneous, at least in cases where the boundary conditions are constant (constant water depth, constant currents). This means that the statistical moments describing the wave field, e.g., the wave spectrum, are shift invariant. The same should then also be true for the SAR image and the respective SAR image variance spectrum. In this section, a method is presented, which identifies cases where this basic property is violated using ERS-2 imagette data. One motivation for this investigation is to detect imagettes, which are contaminated by the following:

- atmospheric phenomena like boundary layer rolls [26], atmospheric fronts, or rain cells [27];
- surface slicks of anthropogenic or biological origin [28];
- sea ice.

Furthermore, the method is able to detect ocean wave fields with strong spatial dynamics, which are not properly described by a spectrum. These inhomogeneities can be due to different phenomena such as the following:

- changing water depth;
- inhomogeneous current fields;
- extreme wave grouping, i.e., large distances between wave groups.

All these features have a spoiling effect on SAR wave measurements and must be detected with high reliability.

According to standard spectral estimation theory, spectral densities estimated from a single periodogram $\hat{\Phi}$ [29] are negative exponentially distributed, i.e., $\mathrm{var}(\hat{\Phi}_k)$ is equal to mean $(\hat{\Phi}_k)^2$ for all wavenumber components k. A standard approach to reduce the variance of the spectral estimator is to average periodograms estimated from subimages. To check the homogeneity of wave mode imagettes, $N = 32$ subimages of about 1×1 km size were used to estimate the mean and variance of the periodogram and to test the above relation between mean and variance of the periodogram. The boxes used for the estimation are shown in Fig. 11. The box size is still large enough to resolve even swell systems. The basic idea of the test is to check whether

$$\frac{\overline{\mathrm{var}}(\hat{\Phi}_k)}{(\overline{\mathrm{mean}}(\hat{\Phi}_k))^2} \approx 1 \quad \text{for all wave number bins } k \tag{51}$$

holds. Here, $\overline{\mathrm{mean}}$ denotes the standard estimator for the mean, and $\overline{\mathrm{var}}$ is an estimator for the variance of the periodogram defined as

$$\overline{\mathrm{var}}(\hat{\Phi}_k) = \frac{1}{N}\sum_{j=1}^{N}\left(\hat{\Phi}_k^j\right)^2 - \overline{\mathrm{mean}}(\hat{\Phi}_k)^2 \tag{52}$$

where $\hat{\Phi}_k^j$ denotes the periodogram of the jth subimage. It should be noted that (51) is approximative even if the mean value is taken on the left side. In fact, it can be shown that the expression is slightly biased toward values smaller than one [30].

To avoid the test to be dominated by speckle noise (which is homogeneous), a weighting with spectral energies is introduced, leading to the following definition of an inhomogeneity parameter ξ_H:

$$\xi_H = \left(\sum_k \overline{\mathrm{mean}}(\hat{\Phi}_k)\right)^{-1} \sum_k \frac{\overline{\mathrm{var}}(\hat{\Phi}_k)}{\overline{\mathrm{mean}}(\hat{\Phi}_k)}. \tag{53}$$

The parameter is a weighted average of the expressions given in (51) over all wave components k.

Fig. 11(B) shows the histogram of the inhomogeneity parameter estimated from a dataset of 30 000 ERS-2 imagettes, which is described in [23], including land and sea ice. It can be seen that the peak of the distribution is slightly smaller than one, which is consistent with the known bias of the expression in (51). To classify the imagettes into classes of homogeneous and nonhomogeneous cases, a threshold of 1.05 was chosen by visual inspection. It turned out that this choice results in a reliable detection of atmospheric fronts, slicks, and sea ice.

ACKNOWLEDGMENT

The complex SAR data were reprocessed from ERS-2 wave mode raw data provided by ESA in the framework of the COMPLEX project.

REFERENCES

[1] W. R. Alpers, D. B. Ross, and C. L. Rufenach, “On the detectability of ocean surface waves by real and synthetic aperture radar,” *J. Geophys. Res.*, vol. 86, pp. 6481–6498, 1981.

[2] D. R. Lyzenga, R. A. Shuchman, and J. D. Lyden, “SAR imaging of waves in water and ice: Evidence for velocity bunching,” *J. Geophys. Res.*, vol. 90, pp. 1031–1036, 1985.

[3] K. Hasselmann, R. K. Raney, W. J. Plant, W. Alpers, R. A. Shuchman, D. R. Lyzenga, C. L. Rufenach, and M. J. Tucker, "Theory of synthetic aperture radar ocean imaging: A MARSEN view," *J. Geophys. Res*, vol. 90, pp. 4659–4686, 1985.

[4] K. Hasselmann and S. Hasselmann, "On the nonlinear mapping of an ocean wave spectrum into a synthetic aperture radar image spectrum," *J. Geophys. Res.*, vol. 96, pp. 10 713–10 729, 1991.

[5] H. Krogstad, "A simple derivation of Hasselmann's nonlinear ocean-synthetic aperture radar transform," *J. Geophys. Res.*, vol. 97, pp. 873–885, 1992.

[6] M. Dowd and P. W. Vachon, "Ocean wave extraction from RADARSAT synthetic aperture radar inter-look image cross spectra," *IEEE Trans. Geosci. Remote Sensing*, vol. 39, pp. 21–37, Jan. 2001.

[7] D. R. Lyzenga, "Unconstrained inversion of waveheight spectra from SAR images," *IEEE Trans. Geosci. Remote Sensing*, vol. 40, pp. 261–270, Feb. 2002.

[8] C. Mastenbroek and C. F. de Valk, "A semi-parametric algorithm to retrieve ocean wave spectra from synthetic aperture radar," *J. Geophys. Res.*, vol. 105, pp. 3497–3516, 2000.

[9] S. Hasselmann, C. Brüning, K. Hasselmann, and P. Heimbach, "An improved algorithm for the retrieval of ocean wave spectra from synthetic aperture radar image spectra," *J. Geophys. Res.*, vol. 101, pp. 16 615–16 629, 1996.

[10] H. Krogstad, O. Samset, and P. W. Vachon, "Generalizations of the nonlinear ocean-SAR transformation and a simplified SAR inversion algorithm," *Atmos. Ocean*, vol. 32, pp. 61–82, 1994.

[11] G. Engen and H. Johnson, "SAR-ocean wave inversion using image cross spectra," *IEEE Trans. Geosci. Remote Sensing*, vol. 33, pp. 1047–1056, July 1995.

[12] L. A. Breivik, M. Reistad, H. Schyberg, J. Sunde, H. E. Krogstad, and H. Johnson, "Assimilation of ERS SAR wave spectra in an operational wave model," *J. Geophys. Res.*, vol. 103, pp. 7887–7900, 1998.

[13] M. Prevosto, H. E. Krogstad, and A. Robin, "Probability distributions for maximum wave and crest heights," *Coastal Eng.*, vol. 40, pp. 329–360, 2000.

[14] W. J. Plant and L. M. Zurk, "Dominant wave directions and significant wave heights from synthetic aperture radar imagery of the ocean," *J. Geophys. Res.*, vol. 102, pp. 3473–3482, 1997.

[15] R. K. Raney and P. W. Vachon, "Synthetic aperture radar imaging of ocean waves from an airborne platform: Focus and tracking issues," *J. Geophys. Res.*, vol. 93, pp. 12 475–12 486, 1988.

[16] O. M. Phillips, *Dynamics of the Upper Ocean*. Cambridge, U.K.: Cambridge Univ. Press, 1977.

[17] C. Brüning, R. Schmidt, and W. Alpers, "Estimation of ocean wave-radar modulation transfer function from synthetic aperture radar imagery," *J. Geophys. Res.*, vol. 99, pp. 9803–9815, 1994.

[18] R. Bamler and B. Schättler, "SAR data acquisition and image formation," in *SAR Geocoding: Data and Systems*: Wichman, 1993.

[19] C. Brüning, W. Alpers, and K. Hasselmann, "Monte-Carlo simulation studies of the nonlinear imaging of a two dimensional surface wave field by a synthetic aperture radar," *Int. J. Remote Sens.*, vol. 11, pp. 1695–1727, 1990.

[20] V. Kerbaol, B. Chapron, and P. W. Vachon, "Analysis of ERS-1/2 synthetic aperture radar wave mode imagettes," *J. Geophys. Res.*, vol. 103, pp. 7833–7846, 1998.

[21] J. W. Goodman, *Statistical Optics*. New York: Wiley, 1985.

[22] W. Alpers and K. Hasselmann, "Spectral signal to clutter and thermal noise properties of ocean wave imaging synthetic aperture radars," *Int. J. Remote Sens.*, vol. 3, pp. 423–446, 1982.

[23] S. Lehner, J. Schulz-Stellenfleth, B. Schättler, H. Breit, and J. Horstmann, "Wind and wave measurements using complex ERS-2 SAR wave mode data," *IEEE Trans. Geosci. Remote Sensing*, vol. 38, pp. 2246–2257, Sept. 2000.

[24] J. Schulz-Stellenfleth, S. Lehner, and D. Hoja, "Use of the coherence of synthetic aperture radar look cross spectra for ocean wave measurements," in *Proc. IGARSS*, Toronto, ON, Canada, 2002.

[25] S. Lehner, J. Horstmann, W. Koch, and W. Rosenthal, "Mesoscale wind measurements using recalibrated ERS SAR images," *J. Geophys. Res.*, vol. 103, pp. 7847–7856, 1998.

[26] W. Alpers and B. Brümmer, "Atmospheric boundary layer rolls observed by the synthetic aperture radar aboard the ERS-1 satellite," *J. Geophys. Res.*, vol. 99, pp. 12 613–12 621, 1994.

[27] C. Melsheimer, W. Alpers, and M. Gade, "Investigation of multi-frequency/multipolarization radar signatures of rain cells over the ocean using SIR-C/X-SAR data," *J. Geophys. Res.*, vol. 103, pp. 18 851–18 866, 1998.

[28] M. Gade, W. Alpers, H. Hühnerfuss, H. Masuko, and T. Kobayashi, "Imaging of biogenic and antropogenic ocean surface films by the multi-frequency/multipolarization SIR-C/X-SAR," *J. Geophys. Res.*, vol. 103, pp. 18 851–18 866, 1998.

[29] J. Honerkamp, *Stochastic Dynamical Systems*. Weinheim, Germany: VCH, 1993.

[30] Ch. Oliver and S. Quegan, *Understanding Synthetic Aperture Radar Images*. Norwood, MA: Artech House, 1998.

[31] WAMDI Group, "The WAM model—A third generation ocean wave prediction model," *J. Phys. Oceanography*, vol. 18, pp. 1775–1810, 1988.

Johannes Schulz-Stellenfleth received the Diploma degree in applied mathematics from the University of Hamburg, Hamburg, Germany, in 1996.

He joined the German Aerospace Center (DLR), Oberpfaffenhofen, Germany, in late 1996. He is currently a Research Scientist with the Remote Sensing Technology Institute (IMF), DLR. The main interest of his present work is the use of complex SAR data to derive two-dimensional ocean wave spectra. Apart from that, he is working on the application of cross track interferometric (InSAR) data to measure sea surface elevation models.

Susanne Lehner (M'01) received the M.S. degree in applied mathematics from Brunel University, Uxbridge, U.K., in 1979, and the Ph.D. degree in geophysics from the University of Hamburg, Hamburg, Germany, in 1984.

She was a Research Scientist with the Max-Planck Institute for Climatology, Hamburg, Germany, and in 1996, she joined the German Aerospace Center (DLR/DFD), Oberpfaffenhofen, Germany. She is currently a Research Scientist in the marine remote sensing at the Remote Sensing Technology Institute (DLR/IFM), working on the development of algorithms determining marine parameters from SAR.